

## **Neutron radiography of particle-laden liquid metal flow driven by an electromagnetic induction pump**

Lappan, T.; Sarma, M.; Heitkam, S.; Trtik, P.; Mannes, D.; Eckert, K.; Eckert, S.;

Originally published:

September 2020

**Magnetohydrodynamics 56(2020)2-3, 167-176**

DOI: <https://doi.org/10.22364/mhd.56.2-3.8>

Perma-Link to Publication Repository of HZDR:

<https://www.hzdr.de/publications/Publ-29867>

Release of the secondary publication  
on the basis of the German Copyright Law § 38 Section 4.

## Neutron radiography of particle-laden liquid metal flow driven by an electromagnetic induction pump

*Tobias Lappan<sup>1\*</sup>, Martins Sarma<sup>1</sup>, Sascha Heitkam<sup>1,2</sup>, Pavel Trtik<sup>3</sup>, David Mannes<sup>3</sup>, Kerstin Eckert<sup>1,2</sup> and Sven Eckert<sup>1\*</sup>*

<sup>1</sup> *Institute of Fluid Dynamics, Helmholtz-Zentrum Dresden-Rossendorf, 01328 Dresden, Germany. \*E-Mail: t.lappan@hzdr.de, s.eckert@hzdr.de*

<sup>2</sup> *Institute of Process Engineering and Environmental Technology, Technische Universität Dresden, 01062 Dresden, Germany.*

<sup>3</sup> *Laboratory for Neutron Scattering and Imaging, Paul Scherrer Institut, 5232 Villigen PSI, Switzerland.*

Ladle metallurgy treatment affects the chemical composition and the impurities in molten steel. To remove non-metallic inclusions, gas injection into the ladle and intense stirring by bubbly flows are essential in the refining process. This paper reports on a model experiment that provides an insight into the bubble–particle interaction in liquid metal at room temperature. We apply neutron radiography as imaging technique for particle-laden liquid metal flow around a cylindrical obstacle representing a single rising bubble. The experimental setup is tailored to both the measurement principle of neutron transmission imaging and the design of the disc-type induction pump driving the flow. A liquid metal loop of  $30 \times 3 \text{ mm}^2$  rectangular cross section is filled with low-melting gallium-tin alloy. Gadolinium oxide particles (0.3–0.5 mm) are employed because of their superior neutron attenuation compared to liquid gallium-tin. The neutron image sequences visualise the particle trajectories in the opaque liquid metal with high temporal resolution (100 fps). Up- and downstream the cylindrical obstacle, we analyse the velocity field as a function of the pump’s rotational speed by particle image velocimetry (PIV). The time-averaged particle velocity measured by PIV is lower than the circumferential velocity of the pump’s discs. This velocity deficit arises from the particles’ buoyancy and the pressure drop in the liquid metal loop. In the further analysis of these neutron image data, we will focus on the fluid flow in the wake of the cylindrical obstacle.

**Introduction** In metallurgy, the control of non-metallic inclusions is one of the main issues for the production of high-performance structural and functional materials like aluminium alloys and steels [1]. In the liquid state, the metals are treated by gas injection into a ladle. The bubble flow stirs the molten bath, forcing the solid inclusions to agglomerate and float upwards up into the slag. In this bubble flotation process, inclusion agglomeration plays an essential role, because the probabilities of collision and attachment between bubbles and inclusions strongly depend on the inclusions’ size distribution [2]. The inclusion capture probability has been predicted to be a function of the bubble size, depending on the bubble shape and on their terminal velocity, under turbulent flow conditions in molten steel [3]. Recent investigations have shown different relevant modes of collision [4].

Due to the high melting temperature of metallic engineering materials and the opaqueness of liquid metals, experimental data on bubble and inclusion interactions in a molten metal bath are scarcely available. For in-situ visualisation of multi-phase flow, transmission imaging employing X-ray or neutron radiation are promising techniques. X-ray radiography has been used to characterise bubbly flows in eutectic gallium-indium-tin alloy [5, 6, 7]. By means of synchrotron-based micro-radioscopy, the motion of particles and liquid has been studied in model

experiments on semi-solid casting of aluminium alloys [8]. Neutron radiography provides novel measurement possibilities for time-resolved imaging of solid particles in liquid metal flows. One of the first experiments has been performed on the dynamic visualisation of millimetre-sized composite particles in liquid gallium. A highly turbulent flow has been electromagnetically induced by a system of four counter-rotating permanent magnets [9, 10].

Electromagnetic induction pumps are used both in technical systems and experimental facilities to drive a circulation of liquid metal – without any moving parts that come in direct contact with the fluid. First electromagnetic pumps, which are based on rotating permanent magnets, have been developed about 20 years ago [11, 12]. More recently, the design and the performance of a disc-type rotating permanent magnet induction pump have been investigated [13].

In this work, neutron radiography is employed to visualise particle-laden liquid metal flow with high temporal resolution. We observe and analyse the fluid flow around a cylindrical obstacle, which represents a single bubble, to demonstrate the particle accumulation in the cylinder wake. In a closed loop, the liquid metal flow is driven by an electromagnetic induction pump employing twin magnet discs. Particle image velocimetry (PIV) is applied to compare the velocity field in the channel and around the obstacle for different pump rotational speeds.

**1. Liquid metal experiment** The flow experiments are carried out in a closed liquid metal loop equipped with an electromagnetic induction pump (Fig. 1). The flat channel made of austenitic stainless steel has a rectangular cross section of 3 mm depth in neutron beam direction, and 30 mm width. A 5 mm diameter cylindrical obstacle, which represents a rigid bubble rising in liquid metal, is placed in the middle of the straight channel section. The disc-type rotating permanent magnet induction pump (Fig. 2) is located at the lower U-shaped channel section (Fig. 1a). The clearance between the magnetic discs equals 11.5 mm, which is the smallest possible value for the employed channel. The discs are rotating in clockwise direction (cf. Fig. 1) with  $15\text{--}34\text{ min}^{-1}$  rotational speed range.

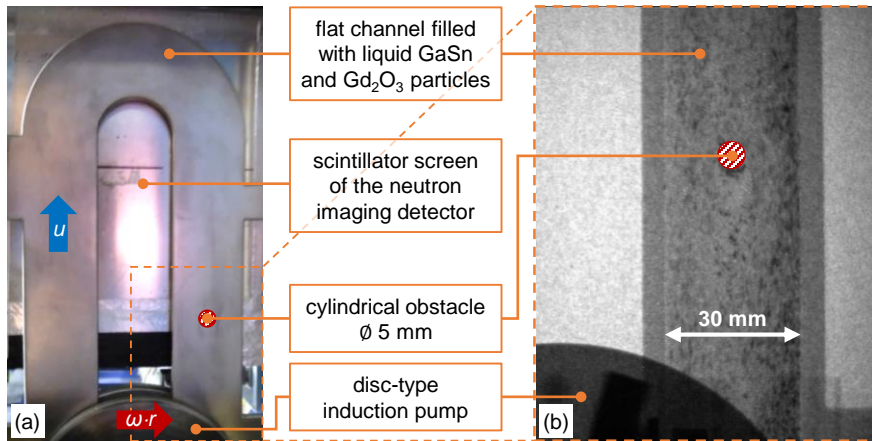


Figure 1: Test arrangement in front of the neutron imaging detector: (a) photograph of the setup; (b) neutron radiograph of particle-laden liquid metal flow in the straight channel section around the cylindrical obstacle.

Low-melting gallium alloyed with 7 wt% tin (GaSn) is employed as model liquid metal, allowing to operate the experimental setup at room temperature

without additional heating. Porous sintered gadolinium oxide particles ( $\text{Gd}_2\text{O}_3$ ) of 0.3–0.5 mm particle size range act as model particles (Fig. 5b). To introduce the particles into the liquid metal, a two-step mixing protocol has been developed. It includes the initial preparation of a paste-like suspensions with high solid content of wetted particles, followed by a second mixing step inside the GaSn-filled channel by means of the electromagnetic pump. Increased rotational speed up to  $550 \text{ min}^{-1}$  combined with alternating rotating direction is applied for intense stirring and distribution of the particles in the liquid metal loop.

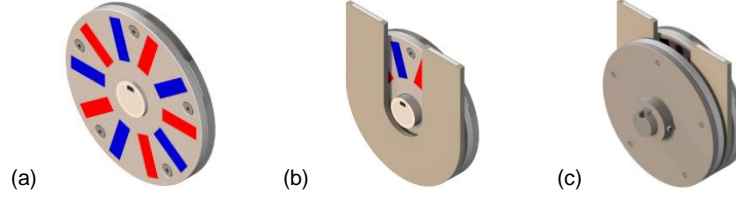


Figure 2: CAD model of the disc-type electromagnetic induction pump. (a) Each disc is equipped with ten permanent magnets ( $\text{NdFeB}$ ,  $V = 30 \times 10 \times 6 \text{ mm}^3$ ,  $B_r = 1.1 \text{ T}$ ), which are arranged with sequentially altering polarities in an aluminium cage screwed together with a ferrous yoke of 120 mm outer diameter. (b) The lower U-shaped channel section of the liquid metal loop is placed (c) between both discs mounted on a low-carbon steel shaft. Opposing magnets are oriented antiparallel.

**2. Neutron transmission imaging** The imaging measurements were performed at the beamlines NEUTRA and ICON (Fig. 3) of the Swiss spallation neutron source (SINQ) [14] at the Paul Scherrer Institut. The neutron energy range – thermal or cold spectrum – determines the contrast achievable and the sample thickness that can be penetrated. For imaging of the particle-laden liquid metal flow, the neutron flux  $\varphi$  is the crucial parameter limiting the temporal resolution. NEUTRA is operated with a constant beam aperture  $D$  of 20 mm, providing approximately  $9.8 \times 10^6 \text{ cm}^{-2} \text{ s}^{-1} \text{ mA}^{-1}$  thermal neutron flux of 25 meV mean energy [15]. Preliminary measurements at the NEUTRA beamline are recorded with 50 fps frame rate. The ICON beamline provides approximately  $42 \times 10^6 \text{ cm}^{-2} \text{ s}^{-1} \text{ mA}^{-1}$  cold neutron flux of 8.5 meV mean energy while using 40 mm beam-defining aperture [16]. These superior neutron flux conditions at ICON allow applying a higher frame rate of 100 fps. During the measurements at NEUTRA and ICON, the neutron source was operated with 1.3 mA proton beam current.

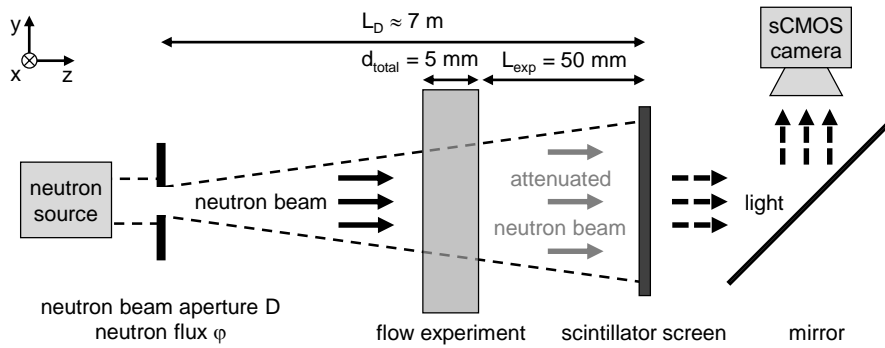


Figure 3: Neutron imaging setup at the beamlines NEUTRA and ICON.

The liquid metal loop was placed close to the scintillator screen of the neutron imaging detector ( $L_{exp} = 50$  mm) at both beamlines (Fig. 3). The distance  $L_D$  between the neutron beam aperture and the screen equalled 7292 mm (NEUTRA) or 6864 mm (ICON). The divergent neutron beam passes through the experimental setup and is strongly attenuated locally by the gadolinium oxide particles, which move within the liquid metal flow. Transmitted neutrons impinge on the  $160 \times 160$  mm<sup>2</sup> scintillator screen (<sup>6</sup>LiF:ZnS, 200  $\mu$ m thickness), emitting visible light after the neutron absorption. The light pattern is recorded by means of a sCMOS camera (Hamamatsu ORCA Flash 4.0, equipped with photographic lens Nikon AF-S NIKKOR 50 mm 1:1.4G), capturing  $100 \times 100$  mm<sup>2</sup> field of view with  $1024 \times 1024$  px<sup>2</sup>. This imaging setup yields time-resolved neutron radiographic image sequences of the two-dimensional particle projections in the liquid metal flow with 0.1 mm image pixel size (Fig. 1b).

The rare-earth element gadolinium offers the largest neutron attenuation coefficient ( $\mu_{Gd} = 1476$  cm<sup>-1</sup>, for 25 meV thermal neutrons) of all stable elements, more than three orders of magnitude higher than gallium ( $\mu_{Ga} = 0.49$  cm<sup>-1</sup>), tin ( $\mu_{Sn} = 0.21$  cm<sup>-1</sup>) or iron ( $\mu_{Fe} = 1.19$  cm<sup>-1</sup>) [17]. Hence, gadolinium-based particles are perfectly suited for time-resolved neutron imaging studies on liquid metal flow [9, 10] as well as on liquid foam and froth [18, 19]. Based on the measurement principle of transmission imaging, which is described by Beer-Lambert's law

$$\frac{I}{I_0} = \exp(-\mu \cdot d_z) \quad (1)$$

the liquid gallium-tin alloy ( $d_{GaSn} = 3$  mm) and the steel channel walls ( $d_{steel} = 2 \cdot 1$  mm) are considered as neutron-transparent since only approximately 30 % of the initial neutron flux is attenuated by these components in total. In contrast, gadolinium oxide particles of 0.05 mm diameter attenuate more than 99.9 % of incoming neutron radiation (Fig. 4) and thus, the particle projections appear as high-contrast spots in the neutron images (Fig. 1b).

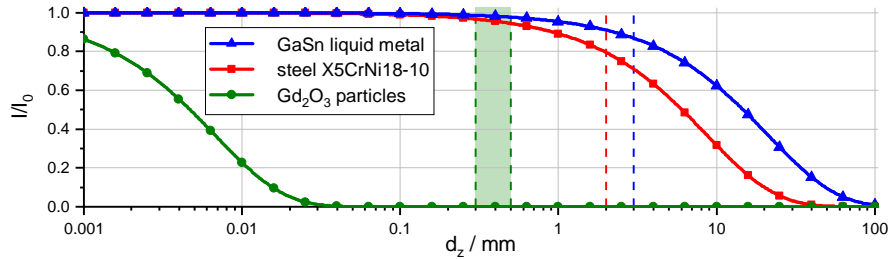


Figure 4: Thermal neutron ( $E = 25$  meV) attenuation characteristics, calculated by Beer-Lambert law: neutron transmittance  $I/I_0$ , depending on the irradiated material and its thickness  $d_z$  along the neutron beam direction.

Even though 0.05 mm particles would be theoretically sufficient, coarser particle fractions of 0.3–0.5 mm diameter are employed, shown in Fig. 5b. This is for three reasons. First, geometrical unsharpness due to the finite aperture of the beamline blurs the projected image of a particle. Second, the movement of the particles and the required exposure time cause an additional blurring of the particle image. And third, the low neutron flux results in high image noise and consequently low contrast-to-noise ratio, especially for smaller particles. Reducing the neutron beam aperture  $D$  decreases the first effect, but also increases noise and required exposure time. Consequently, preliminary tests are conducted to optimize particle size and exposure time for a given beamline and imaging setup.

**3. Results and Discussion** In preliminary neutron imaging measurements at the beamlines NEUTRA and ICON, the contrast-to-noise ratio has been evaluated depending on both the image exposure time and the particle diameter (Fig. 6, Fig. 7). For several particle fractions in the size range  $d_p = 0.1 - 0.5$  mm, a few single gadolinium particles (Fig. 5a) are imaged. To avoid any contrast reduction due to motion blurring, the particles are immobile in front of the 3 mm GaSn-filled flat channel.

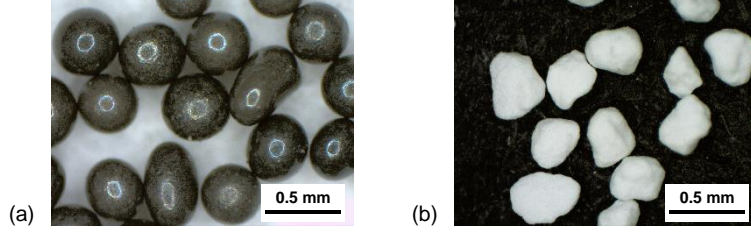


Figure 5: Stereo-microscopic images of neutron-opaque (a) gadolinium (Gd) and (b) gadolinium oxide ( $\text{Gd}_2\text{O}_3$ ) particles.

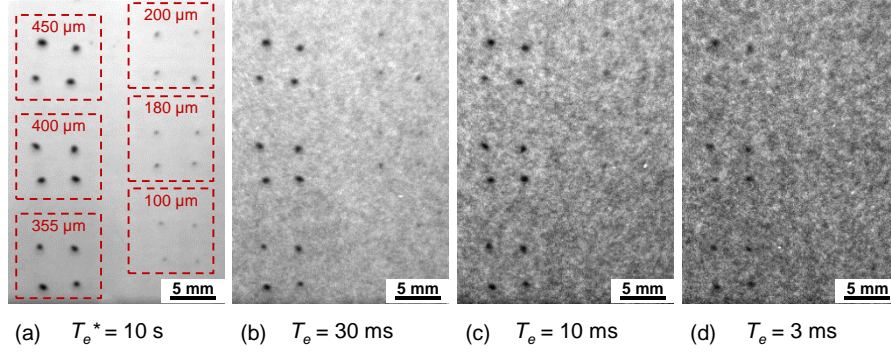


Figure 6: Preliminary neutron imaging measurements to evaluate the contrast-to-noise ratio of gadolinium particles, depending on the particle diameter  $d_p$  and the image exposure time  $T_e$ , at the ICON beamline.

Image contrast refers to the signal difference between a single gadolinium particle and the local background, which results from the neutron attenuation in the liquid GaSn alloy and the steel channel walls. Contrast-to-noise  $CNR$  is defined as the ratio of this signal difference to the noise level

$$CNR = \frac{|\tilde{I}_{min} - \tilde{I}_{mean}|}{\tilde{I}_{\sigma}} \quad (2)$$

with the minimum signal  $\tilde{I}_{min}$  in the particle's centre, the mean background signal  $\tilde{I}_{mean}$  next to the particle and its standard deviation  $\tilde{I}_{\sigma}$  in the greyscale image. As a quantitative metric,  $CNR$  describes how much the signal difference between individual particles and background rises above statistical pixel-to-pixel variations in the background.

Comparing the achieved contrast-to-noise ratio at both beamlines NEUTRA and ICON, Fig. 7 gives generally higher  $CNR$  values for a given particle diameter and image exposure time at ICON due to the increased neutron beam aperture and thus, higher cold neutron flux. At the NEUTRA beamline, gadolinium particles of 0.3–0.5 mm diameter yield  $CNR < 2.0$  in case of  $T_e = 10$  ms (Fig. 7a), but at ICON the contrast-noise-ratio exceeds 4.0 for the same image exposure time (Fig. 7b). Extending the image exposure time reduces the image noise level  $\tilde{I}_\sigma$  (Eq. (2), cf. Fig. 6) and thus, increases the contrast-to-noise ratio. However, to image individual particles moving with the liquid metal flow and to minimise motion blurring, the neutron image sequences are captured with 100 fps frame rate corresponding to 10 ms image exposure time.

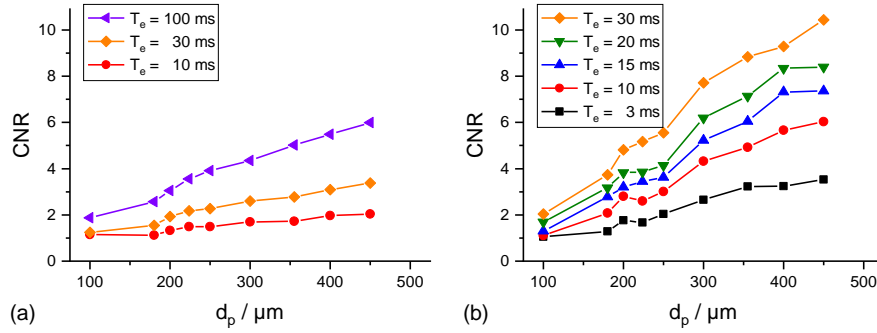


Figure 7: Contrast-to-noise ratio of gadolinium particles, depending on the particle diameter  $d_p$  and the image exposure time  $T_e$ , at the beamlines (a) NEUTRA ( $\varphi = 9.8 \times 10^6 \text{ cm}^{-2} \text{ s}^{-1} \text{ mA}^{-1}$ ) and (b) ICON ( $\varphi = 42 \times 10^6 \text{ cm}^{-2} \text{ s}^{-1} \text{ mA}^{-1}$ ).

Imaging the flow experiment, the neutron image sequences show the projections of the neutron-opaque gadolinium oxide particles moving in the liquid metal loop. Particle image velocimetry [20] is employed to determine the velocity of the particles. A time-resolved PIV algorithm with sliding sum-of-correlation within the software DaVis 10 (LaVision, Göttingen) is applied to analyse sequences of 1500 images. The resulting velocity field is assumed to resemble the velocity of the liquid metal flow driven by the electromagnetic induction pump. Depending on the pump rotational speed  $\omega$ , Fig. 8 maps the time-averaged velocity field  $\bar{\mathbf{u}}$  in the straight channel section of the liquid metal loop, in particular around the cylindrical obstacle. The fluid flow in the cylinder wake is characterised by a significantly lower magnitude of the local velocity.

The time-averaged velocity field is not symmetrically in the left ( $x < 0$  mm) and right ( $x > 0$  mm) half of the imaged channel section. Figure 9a shows the time-averaged profile of the vertical velocity component  $\bar{u}_y$  across the channel width upstream of the cylindrical obstacle ( $-25 \text{ mm} < y < -15 \text{ mm}$ ). The mean value of the velocity magnitude has small fluctuations along the flow path, represented by the error bars. In addition, the inhomogeneous distribution of the velocity across the channel width with decreasing pump speed is visible. Figure 9b depicts mean value and spatial variation of the vertical velocity, derived from Fig. 9a. Additionally, Fig. 9b compares this velocity to the circumferential velocity of the magnet discs at the inner  $r_i = 25$  mm and outer radius  $r_o = 50$  mm covering the U-shaped flat channel. The mean particle velocity obtained by PIV is 20–30 % lower than the circumferential velocity of the magnet discs in the centre line of the channel. This velocity deficit could result from two effects.



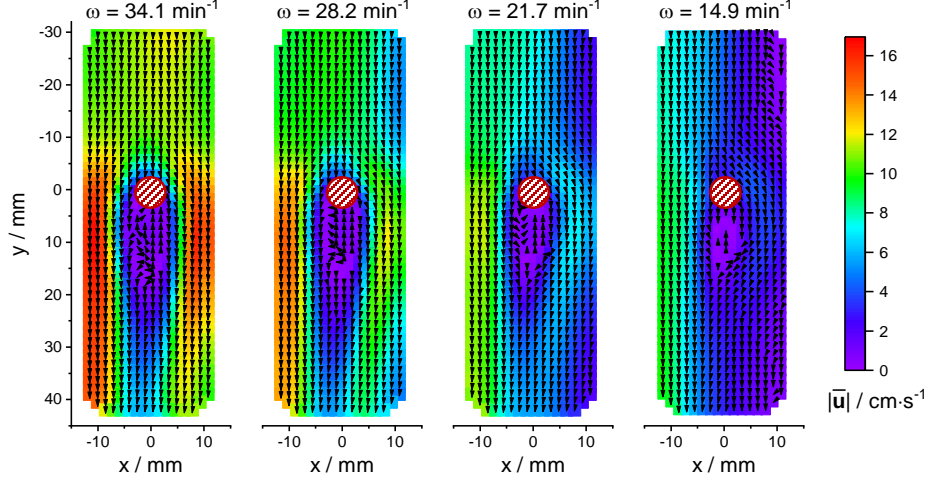


Figure 8: Particle image velocimetry of particle-laden liquid metal flow in the straight channel section around the cylindrical obstacle: time-averaged velocity field  $\bar{\mathbf{u}}$ , depending on the pump rotational speed  $\omega$ .

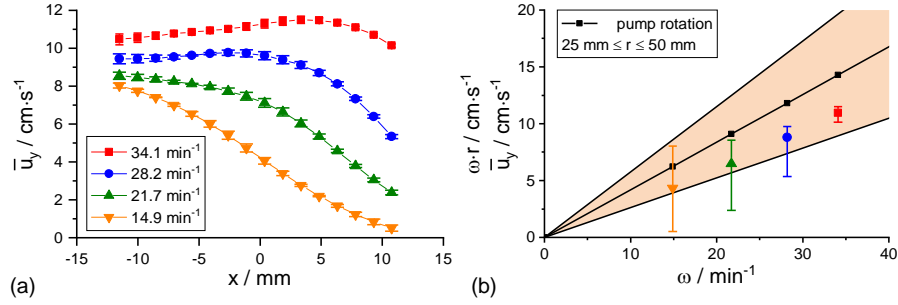


Figure 9: Velocity profile  $\bar{u}_y(x)$  (a) across the channel upstream of the cylindrical obstacle and (b) compared to the estimated velocity range depending on the pump rotational speed  $\omega$ . The legend of the symbols used in (a) also applies to (b).

First, the particles are not neutrally buoyant, resulting in a terminal velocity difference between particle and fluid. The terminal velocity  $v_r$  is calculated by taking the drag coefficient  $c_d$  of the particle and its Reynolds number  $Re$  into account [21].

$$v_r = \sqrt{\frac{4}{3} \cdot \frac{g \cdot d_p}{c_d} \cdot \left( \frac{\rho_p}{\rho_l} - 1 \right)} \quad (3)$$

$$c_d = \frac{21}{Re} + \frac{6}{\sqrt{Re}} + 0.28 \quad \text{with} \quad Re = \frac{\rho_l \cdot v_r \cdot d_p}{\eta_l} \quad (4)$$

Assuming spherical gadolinium oxide particles of  $d_p = 0.3\text{--}0.5\text{ mm}$  diameter and  $\rho_p = 5.62\text{ g cm}^{-3}$  bulk density, the estimated rising velocity in liquid gallium-tin alloy ( $\rho_l = 6.16\text{ g cm}^{-3}$ ,  $\eta_l = 2.1\text{ mPa s}$ ) equals  $v_r = 0.8\text{--}1.5\text{ cm s}^{-1}$ . Because of agglomeration, larger particle clusters of 1 mm diameter could reach more than  $3\text{ cm s}^{-1}$ , which is in good agreement with the observed discrepancy in Fig. 9b. Also formation of loose particle trains has been reported as a mechanism to speed up settling processes [22].



Second, the velocity magnitude of the liquid metal could indeed show a deficit to the rotational velocity of the magnetic discs. Since the flow in the thin channel causes significant viscous dissipation, a pressure drop of 200–300 Pa has to be compensated by the electromagnetic induction pump. This is related to a certain slip between liquid metal and magnetic field [13].

**4. Summary** Neutron radiography has been recently introduced as novel imaging technique for liquid metal flow carrying solid tracer particles. We apply this technique to visualise particle-laden liquid metal flow around a cylindrical obstacle representing a single rising bubble in a flat channel. Using particle image velocimetry, the neutron image sequences give a unique insight into the flow field of the opaque fluid flow. To achieve a sufficient contrast-to-noise ratio while imaging with high temporal resolution of 100 fps frame rate, the ICON beamline at the Paul Scherrer Institut is employed for the model experiments.

The test arrangement consists of a liquid metal loop, which is filled with liquid gallium-tin alloy at room temperature and driven by an electromagnetic induction pump with different rotational velocities. Tracer particles from gadolinium oxide (0.3–0.5 mm diameter) offer superior neutron attenuation, but also certain restrictions. Due to their comparatively large size, these particles are not able to follow the liquid metal flow perfectly. In addition, the gadolinium oxide particles have a slightly lower mass density than the gallium-tin alloy. Consequently, the particles’ buoyancy yields a systematic underestimation of the fluid velocity. Time-resolved neutron imaging combined with PIV analysis allows to measure the velocity field upstream and downstream the cylindrical obstacle spatially resolved. Further data analysis of the neutron images will be focussed on particle tracking velocimetry applied to individual particles in the cylinder’s wake. We intend to estimate local shear rates and identify particle collisions, potentially leading to agglomeration.

**Acknowledgements** The support provided by the Agence nationale de la recherche (ANR-15-CE08-0040) and by the Deutsche Forschungsgemeinschaft (DFG-284002692) is gratefully acknowledged. This work is based on experiments performed at the Swiss spallation neutron source of the Paul Scherrer Institut. We would like to thank Michael Knobel for measuring the mass density of the gadolinium oxide particles.

## References

1. L. ZHANG AND B. G. THOMAS. State of the art in evaluation and control of steel cleanliness. *ISIJ International*, vol. 43 (2003), no. 3, pp. 271–291.
2. L. ZHANG AND S. TANIGUCHI. Fundamentals of inclusion removal from liquid steel by bubble flotation. *International Materials Reviews*, vol. 45 (2000), no. 2, pp. 59–82.
3. H. DUAN, Y. REN, AND L. ZHANG. Modeling of turbulent flow around bubbles in molten steel. *steel research international*, vol. 90 (2019), no. 6, p. 1800576. Citation Key Alias: duan2019.
4. A.-E. SOMMER, ET AL. A novel method for measuring flotation recovery by means of 4d particle tracking velocimetry. *Minerals Engineering*, vol. 124 (2018), pp. 116–122. Tex.publisher: Elsevier BV.
5. N. SHEVCHENKO, ET AL. Application of X-ray radiosopic methods for characterization of two-phase phenomena and solidification processes in metallic melts. *The European Physical Journal Special Topics*, vol. 220 (2013), no. 1, pp. 63–77.
6. O. KEPLINGER, N. SHEVCHENKO, AND S. ECKERT. Validation of X-ray radiography for characterization of gas bubbles in liquid metals. *IOP Conference Series: Materials Science and Engineering*, vol. 228 (2017), p. 012009.

7. M. AKASHI, ET AL. X-ray radiosopic visualization of bubbly flows injected through a top submerged lance into a liquid metal. *Metallurgical and Materials Transactions B*, (2019).
8. S. ZABLER, ET AL. Particle and liquid motion in semi-solid aluminium alloys: A quantitative in situ microradioscopy study. *Acta Materialia*, vol. 61 (2013), no. 4, pp. 1244–1253.
9. M. SCEPANSKIS, ET AL. A report on the first neutron radiography experiment for dynamic visualization of solid particles in an intense liquid metal flow. *Magnetohydrodynamics*, vol. 51 (2015), no. 2, pp. 257–265.
10. M. SARMA, ET AL. Neutron Radiography Visualization of Solid Particles in Stirring Liquid Metal. *Physics Procedia*, vol. 69 (2015), pp. 457–463.
11. I. E. BUCENIEKS, E. P. SUKHOVICH, AND E. V. SHCHERBININ. A centrifugal pump basing on rotating permanent magnets. *Magnetohydrodynamics*, vol. 36 (2000), no. 2, pp. 157–164.
12. I. E. BUCENIEKS. Perspectives of using rotating permanent magnets in the design of electromagnetic induction pumps. *Magnetohydrodynamics*, vol. 36 (2000), no. 2, pp. 151–156.
13. E. KOROTEEVA, M. SCEPANSKIS, I. BUCENIEKS, AND E. PLATACIS. Numerical modeling and design of a disk-type rotating permanent magnet induction pump. *Fusion Engineering and Design*, vol. 106 (2016), pp. 85–92.
14. B. BLAU, ET AL. The Swiss Spallation Neutron Source SINQ at Paul Scherrer Institut. *Neutron News*, vol. 20 (2009), no. 3, pp. 5–8.
15. E. H. LEHMANN, P. VONTOBEL, AND L. WIEZEL. Properties of the radiography facility NEUTRA at SINQ and its potential for use as european reference facility. *Nondestructive Testing and Evaluation*, vol. 16 (2001), no. 2-6, pp. 191–202.
16. A. P. KAESTNER, ET AL. The ICON beamline - A facility for cold neutron imaging at SINQ. *Nuclear Instruments and Methods in Physics Research Section A - Accelerators, Spectrometers, Detectors and Associated Equipment*, vol. 659 (2011), no. 1, pp. 387–393.
17. F. GRÜNAUER. Design, optimization and implementation of the new neutron radiography facility at FRM-II. PhD thesis, Technische Universität München, München, 2005.
18. S. HEITKAM, ET AL. Neutron imaging of froth structure and particle motion. *Minerals Engineering*, vol. 119 (2018), pp. 126–129.
19. S. HEITKAM, ET AL. Tracking of Particles in Froth Using Neutron Imaging. *Chemie Ingenieur Technik*, vol. 91 (2019), no. 7, pp. 1001–1007.
20. M. RAFFEL, ET AL. *Particle Image Velocimetry: A Practical Guide* (Springer International Publishing, Cham, 2018).
21. H. KÜRTEEN, J. RAASCH, AND H. RUMPF. Beschleunigung eines kugelförmigen Feststoffteilchens im Strömungsfeld konstanter Geschwindigkeit. *Chemie Ingenieur Technik*, vol. 38 (1966), no. 9, pp. 941–948.
22. S. HEITKAM, ET AL. Speeding up of sedimentation under confinement. *Physical Review Letters*, vol. 110 (2013), no. 17, p. 178302.